International Journal of Fluid Machinery and Systems
Vol. 5, No. 3, July-September 2012

DOI: http://dx.doi.org/10.5293/IJFMS.2012.5.3.117
ISSN (Online): 1882-9554

Original Paper

Aspect-Ratio Effects and Unsteady Pressure Measurements inside a Cross-Flow Impeller

Katsuya Hirata, Yusuke Onishi[1], Shigeya Nagasaka, Ryo Matsumoto and Jiro Funaki

Department of Mechanical Engineering, Doshisha University
Kyoto 610-0321, Japan, khirata@mail.doshisha.ac.jp

Abstract

In the present experimental study, the authors try to clarify the characteristics of the flow around and inside a cross-flow impeller in a typical geometry, over a wide parameter range of an aspect ratio L/D_2. In order to eliminate the complicated casing factors, the impeller rotates in open space without any casings. As a result, by using hot wire anemometer measurements and by conventional flow visualisations with a particle image velocimetry technique, the authors show that both the outflow rate and the maximum vorticity attain the maximum for $L/D_2 = 0.6$. In order to investigate the aspect-ratio effect, we further reveal minute fluctuating pressures on an impeller end wall for a singular $L/D_2 = 0.6$. Especially in these pressure measurements, the eccentric vortex is prevented to revolute by the insertion of a tongue, in order to consider the spatial structure of flow more precisely.

Keywords: *Cross-Flow Fan, Blower, Fan, Aspect Ratio, Pressure Measurement*

1. Introduction

For further improvement of indoor environments against air and noise pollutions, smarter ventilation is one of the key factors. As a ventilation device, the cross-flow fan, or the cross-flow impeller, has been widely used for industrial equipments and home electric appliances like air curtains and air conditioners, in spite of its rather lower efficiency and higher sound-noise level. Because, the cross-flow impeller can easily generate almost uniform, two-dimensional, thin and wide flow in the direction perpendicular to its axis (see Eck (1973) [1]).

Until now, many experimental and analytical researches have been conducted [1] – [21]. Recently, applications to aircraft propulsion and flow control have been actively pursuing [22] and [23]. But, most of them are related with long-span cross-flow impellers due to their practical advantage of two-dimensional flow. Here, 'long-span' means that aspect ratio $L/D_2 \gtrsim 1$. On the other hand, researches of a thin cross-flow impeller which has a short axis of $L/D_2 \ll 1$ have not yet been reported, in spite of recent requirements in micro electronical packaging and so on. Recently, we have investigated a thin cross-flow impeller which has a short axis [24]. The study shows a high potential in micro electronical packagings and so on. Besides, we have reported the blade-surface-pressure measurements of a simple-blade impeller, as well [25].

In this study, we try to clarify the characteristics of the flow around and inside a cross-flow impeller in a typical geometry, over a wide range of the aspect ratio L/D_2, referring to our previous study [24]. Concretely speaking, for various values of L/D_2 we experimentally investigate the flow using measurements by a hot wire anemometer (hereinafter, referred to as HWA) and conventional flow visualisations together with partical image velocimetry (hereinafter, referred to as PIV) analyses. In order to investigate the aspect-ratio effect, we further reveal minute fluctuating pressures on an impeller end wall for a singular $L/D_2 = 0.6$. Especially in these pressure measurements, the eccentric vortex is prevented to revolute by the insertion of a tongue, in order to consider the spatial structure of flow more precisely. –In the present paper, the word "revolution" means the rotation with regard to the eccentric vortex, in order to avoid the confusion with the rotation with regard to the impeller. –

In order to eliminate complicated factors that can influence the flow characteristics, the impeller rotates in open space without any casings, as well as our previous studies [24] and [25]. Because, the impeller without any casings could be one of the simplest cross-flow impellers, and the best for basic researches. In general, cross-flow impellers have some complicated casings, so it is difficult to estimate their fundamental characteristics. In addition, concerning the eccentric-vortex revolution phenomenon which will be explained later, the phenomenon not only is interesting due to its strong nonlinearity with flow separation and very different time scales, but also involves practical engineering potentials such as the smart control of the air-conditioner's flow direction.

Complimentarily speaking, in spite of many previous researches [1] – [25], the outer-and-internal flow of the cross-flow impeller has not been clear yet, because of the inherent complexity of the flow separation with strong nonlinearity. Although

Received May 21 2012; Accepted for publication April 17 2012: Paper number O12011S
Corresponding author: Katsuya Hirata, Professor, khirata@mail.doshisha.ac.jp

This paper was presented at 11th Asian International Conference on Fluid Machinery (AICFM) and 3rd Fluid Power Technology Exhibition, November 21-23, 2011, Chennai, India

numerical approaches have been becoming a powerful tool due to the recent development of computer resources, their accuracy can not be guaranteed without accompanying experimental studies.

Among concerning physical quantities, unsteady pressures on the rotating impellers give the useful information for flow and sound-noise level. Besides, such accurate and reliable pressure information was needed as the benchmark for numerical approaches. However, there have been a few accurate works, due to technical difficulties such as the much smaller pressure-fluctuation amplitude than blowers and compressors, and the blade rotation.

2. Experimental Method

2.1 Model

Figure 1 shows the present model, an impeller with forward-cambered (or forward-curved) blades. The similar two impellers in different scales were tested. The smaller one with D_2 = 100 mm is for flow visualisations and flow-velocity measurements, and the other one with D_2 = 250 mm is for pressure measurements. Tables 1 and 2 summarise the detailed dimensions of the impeller. That is, in Table 1, we show the main parameters in aspect-ratio effect where the impeller outer diameter D_2 = 100 mm. And, in Table 2, we show the main parameters in unsteady pressure measurements where D_2 = 250 mm . The model is one of the typical impellers; namely, a forward-cambered-blade impeller. The inclination of the blades is forward, to stabilise the eccentric vortex. In this study, the direction of impeller rotation is clockwise at any time.

We investigate twelve kinds of impellers with different values of the span length L. Important non-dimensional geometrical parameters are as follows: inner-to-outer diameter ratio D_1/D_2 = 0.76, aspect ratio L/D_2 = 0.1 – 5.8. for the aspect-ratio effects and L/D_2 = 0.6 for the unsteady pressure measurements. A non-dimensional kinematical parameter is the Reynolds number, which is defined as follows.

$$Re = \frac{u_2 c}{\nu} \tag{1}$$

where u_2, c and ν are an outer-periphery velocity of the impeller, a chord length of the blade and kinetic viscosity, respectively. Tested Re is in the range of 1.0×10^3 – 5.0×10^3 for the aspect-ratio effect, and in the range of 1.0×10^3 – 8.0×10^3 for the unsteady pressure measurements.

The working fluid is air. A model is installed between two end plates, which are two square transparent acrylic plates. Impellers are made of transparent acrylic plates, in order to observe the flow inside the impeller. More specifically, the impeller consists of 24 transparent blades, one transparent end disc and one black-painted end disc. Here, the end-disc surface coincides with the end-plate surface, and the gap between the end disc and the end plate is very narrow.

2.2 Coordinate system

Figure 2 shows the present coordinate system, which is a cylindrical one (r, θ, z). The origin O is at the impeller centre on the mid-span plane. Especially in the pressure measurements, the eccentric vortex is prevented to revolute by the insertion of a tongue. Note that the tongue is fixed at θ = 0 deg. To detect the value of θ, we use a laser sensor together with a target on the pressure-sensor-mounted blade.

2.3 Hot wire anemometer

In order to know fluctuating flow velocities with high accuracy and high reliability, we conduct HWA measurements using KANOMAX CTA MODEL1008. The HWA is calibrated by the simultaneous steady flow measurement with a Pitot tube. A hot wire probe of type I is put on the position of $2r/D_2$ = 0.55 (r = 55 mm) on the mid-span plane (z/D_2 = 0), as shown in Fig. 3. The hot wire is made from a tungsten wire of 5 μm in diameter and 2 mm in length. Considering the dominant flow direction near the impeller, we put the hot wire parallel to the impeller axis. Because axial velocity component is usually very small.

2.4 Flow visualisation and PIV

For the observation of a whole velocity field, we conduct conventional flow visualisations by smoke and their PIV analyses. We use minute particles of olive oil as tracers. The diameter of smoke particles is in order of 10^{-6} m, and the corresponding Stokes number is 10^{-3} – 10^{-2}. Then, traceability of the present particles is adequate.

2.5 Pressure measurement

The diaphragm of a pressure sensor (SSK, P310W-50) is mounted flash-surfacely on an impeller end wall (see Fig. 3). Its reference pressure is introduced from open air outside the impeller near the impeller center, using a PVC tube. The lowest eigen frequency of the diaphragm is 1.2 kHz, whose response is enough high to measure the fluctuations related with the impeller rotation of 0.55 – 4.4 Hz accurately.

As a preliminary experiment, the calibration of the pressure sensor is carried out, where the static pressure inside the PVC tube is controlled instead of the open air pressure, with in the range of about ±102 Pa. The static pressure is simultaneously monitored using a deadweight pressure gauge. Although the impeller rotates, all equipments cannot be mounted for the pressure measurement on the impeller. In such a situation, the slip ring is conventionally used. However, in the present measurements, a radio telemeter (KYOWA, MRT-301A) is used instead, because the slip ring generates some fatal noises especially synchronised with the impeller rotation.

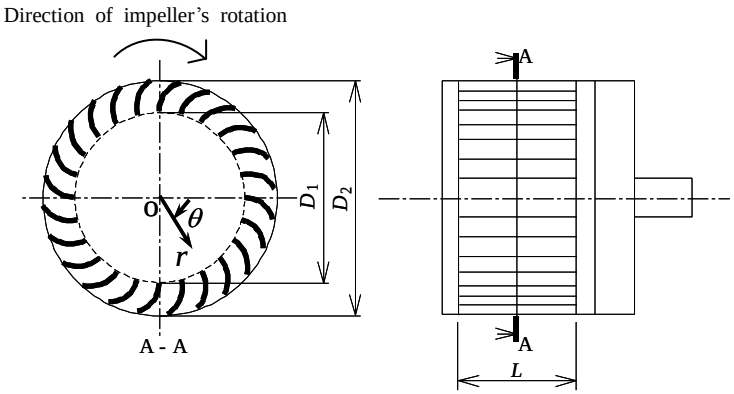

Fig. 1 Model; an impeller with forward-cambered blades.

Table 1 Parameters of an impeller in aspect-ratio-effect investigation.

Outer diameter	D_2 = 100 mm
Inner diameter	D_1 = 76 mm
Number of blades	Z = 24
Chord length	c = 14.3 mm
Blade angles	β_2 = 23 deg, β_1 = 90 deg
Thickness	t = 2 mm
Impeller lengths	L = 10, 20, 30, 40, 50, 60, 70, 100, 200, 300, 500, 580 mm
Aspect ratios	L/D_2 = 0.1, 0.2, 0.3, 0.4, 0.5, 0.6, 0.7, 1.0, 2.0, 3.0, 5.0, 5.8
Blade aspect ratios	L/c = 0.7, 1.4, 2.1, 2.8, 3.5, 4.2, 4.9, 7.0, 14.0, 21.0, 35.0, 40.6
Impeller rotation speed	n = 3.4 – 17.1 Hz (205 – 1025 rpm)
Reynolds numbers	Re = 1.0×10^3– 5.0×10^3

Table 2 Parameters of an impeller in unsteady pressure measurements.

Outer diameter	D_2 = 250 mm
Inner diameter	D_1 = 190 mm
Number of blades	Z = 24
Chord length	c = 35.8 mm
Blade angles	β_2 = 23 deg, β_1 = 90 deg
Thickness	t = 5 mm
Impeller length	L = 150 mm
Aspect ratio	L/D_2 = 0.6
Blade aspect ratio	L/c = 4.2
Impeller rotation speed	n = 0.55 – 4.4 Hz (33 – 260 rpm)
Reynolds numbers	Re = 1.0×10^3 – 8.0×10^3
Measuring position	r/R = 0.22, 0.28, 0.33, 0.34, 0.40, 0.46, 0.50, 0.56, 0.62

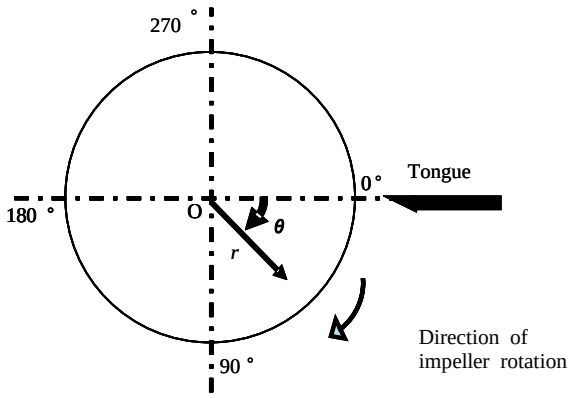

Fig. 2 Coordinate system of an impeller for unsteady pressure measurements.

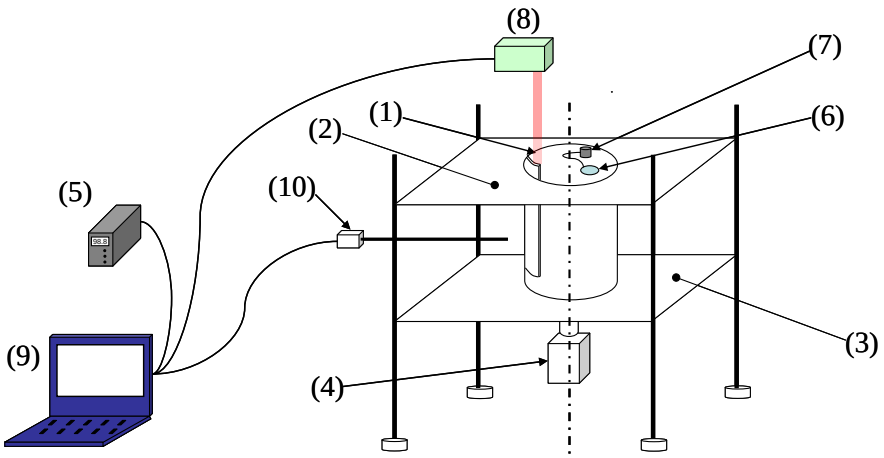

Fig. 3 Experimental apparatus for velocity and pressure measurements. (1) Impeller, (2) side wall (top), (3) side wall (bottom), (4) speed control motor, (5) radio telemeter (receiver), (6) pressure sensor, (7) radio telemeter (transmitter), (8) laser sensor, (9) PC, (10) hot wire probe.

3. Results and Discussion

3.1 Flow around/inside an impeller

Figure 4 shows an example of visualised flows using a conventional flow visualisation technique by smoke, together with a schematic diagram of the flow on its right hand. The flow is for $L/D_2 = 1.0$ and $Re = 2.5\times10^3$. In this study, the rotational direction of the impeller is always clockwise.

In general, it seems difficult to recognise the flow such as the schematic diagram, directly from a still photo on the left hand of Fig. 4. But, from a video camera image, which are a temporally-consecutive series of still photos and their PIV results, we clearly see such schematic flow features, namely, both the eccentric vortex and the in/out flows related with the cross flow. In addition, we can observe a steady revolution of the eccentric vortex in some cases. The revolution speed is much lower than the impeller rotation speed (as will be shown in Fig. 9).

Referring to these observations, we divide the flow field around the impeller periphery into three areas; namely, inflow, outflow and lessflow areas. In Fig. 4, these areas are described as areas i, ii and iii, respectively.

3.2 Aspect-ratio effects

The accuracy of the PIV measurement is unstable and not high. So, we now check it in comparison with the HWA measurements. Then, we can precisely obtain quantitative results by the PIV analyses. So, we define both the outflow rate Q_o out of the impeller and the maximum vorticity ω_{max}, as total indicators of the impeller performance. Q_o is the outflow rate per unit impeller span, which is obtained by a circuit integral of only outflow velocity (excluding inflow velocity) on the outer impeller periphery in the area ii.

Figure 5 shows Q_o plotted against L/D_2. Q_o is non-dimentionalised using flow rate coefficient defined by $C_{Qo} \equiv Q_o/(\omega D_2 u_2)$. We can see that C_{Qo} is almost constant against L/D_2 for $L/D_2 \gtrsim 1$. On the other hand, for $L/D_2 \lesssim 1$, C_{Qo} attains the maximum value for $L/D_2 = 0.6$. In addition, we can see the influence of Re upon C_{Qo}, if we compare the results with different values of Re. From a quantitative viewpoint, C_{Qo} tends to increase with increasing Re. –Complementally speaking, solid circles denote the results in our previous study [22]. As the results are close to the present results, we can confirm the present experimental accuracy, again.–

Figure 6 shows ω_{max} plotted against L/D_2. We can see that ω_{max} is almost constant against L/D_2 for $L/D_2 \gtrsim 1$. On the other hand, for $L/D_2 \lesssim 1$, ω_{max} attains the maximum value for $L/D_2 = 0.6$. In addition, we can see the influence of Re upon ω_{max}, if we compare the results with different values of Re. From a quantitative viewpoint, ω_{max} tends to increase with increasing Re.

To conclude, both C_{Qo} and ω_{max} attain the maximum values for $L/D_2 = 0.6$, respectively. From a practical point of view, these results suggest possibility of more efficient impellers, if we consider the optimum aspect ratio of $L/D_2 = 0.6$.

3.3 Unsteady pressure on an impeller end wall

In order to investigate the aspect-ratio effects further, we reveal minute fluctuating pressures on an impeller end wall at a singular $L/D_2 = 0.6$. The pressure measurements are carried out using a similar large model with $D_2 = 250$ mm instead of the small model with $D_2 = 100$ mm used in Subsections 3.1 and 3.2. Especially in some cases of the pressure measurements, the eccentric vortex is prevented to revolute by the insertion of a tongue, in order to consider the spatial structure of flow linking other

experiments such as flow visualisations and HWA measurements.

At first, we consider the impeller without a tongue. Figure 7 shows the time history of the raw pressure-sensor signal, namely, the surface pressure on an impeller's end wall at $2r/D_2 = 0.62$ for $Re = 8.0\times10^3$. And, Fig. 8 shows the corresponding fast Fourier transform (FFT) analysis of Fig. 7.

In Fig. 7, a dominant oscillation appears with a period of about 0.2 s, together with high-frequency random noises. It can be considered that the periodicity is owing to the impeller rotation whose speed n is 4.4 Hz. More exactly, the dominant frequency is considered to be slightly less than $n = 4.4$ Hz, because of the eccentric-vortex revolution. In fact, Fig. 8 shows that the dominant frequency is equal to 4.2 Hz. Then, the eccentric-vortex-revolution frequency f_{EV} can be evaluated to be the difference 0.2 Hz. Of course, we can support this evaluation by flow visualisations and HWA measurements.

Figure 9 shows the normalised eccentric-vortex-revolution frequency f_{EV}/n averaged over a range of $2r/D_2 = 0.22 – 0.62$ plotted against Re. Each error bar in the figure represents a scattering range. We should note that there exists no plots at $Re = 1.0\times10^3$, because we cannot detect any dominant frequencies owing to the impeller rotation. We can see that f_{EV}/n almost keeps a constant value of about 0.01, being independent of Re.

Furthermore, in Fig. 8, other spectral peaks appear at 120 – 130 Hz, which are much weaker than that of 4.2 Hz and its harmonics. These spectral-peak frequencies coincide with eigen structural frequencies of the present experimental apparatus itself.

Secondly, we consider the impeller with a tongue. Figure 10 shows the time history of the raw pressure-sensor signal, namely, the surface pressure on an impeller end wall at $2r/D_2 = 0.62$ for $Re = 8.0\times10^3$. And, Fig. 11 shows the corresponding fast Fourier transform (FFT) analysis of Fig. 10.

In fig. 10, as well as Fig. 7, a dominant oscillation appears with a period of about 0.2 s, together with high-frequency random noises. In contrast to Fig. 7, the periodicity owing to the impeller rotation is exactly equal to 4.4 Hz in Fig. 10, because of the lack of the eccentric-vortex revolution. In fact, Fig. 11 shows that the dominant frequency is equal to 4.4 Hz. Of course, we can support the no eccentric-vortex revolution by flow visualisations and HWA measurements. –Complimentarily speaking, the periodicity with a tongue seems better than that without a tongue, if we compare Figs. 10 and 11 with Figs. 7 and 8. –

Furthermore, in Fig. 11, as well as Fig. 8, other spectral peaks appear at 120 – 130 Hz, which is much weaker than that of 4.4 Hz and its harmonics.

Figure 12 shows an example of one-period time histories of the surface pressures p_{PA} which are conditionally-averaged over 20 periods on an impeller's end wall. Specifically speaking, Fig. 12 shows a phase-averaged pressure distribution during one impeller-rotation period at $2r/D_2 = 0.62$ for $Re = 8.0\times10^3$. The abscissa is azimuthal position θ of the pressure sensor, instead of time τ, in order to make the spatial understanding easier. In the present study, $\theta = 360$ deg. corresponds to $\tau = 0.23$ s. We can see the pressure in the inflow area i at $\theta \approx 0 – 180$ deg. and the suction in the outflow area ii at $\theta \approx 180 – 360$ deg.

We should note that the negative peak value of p_{PA} in Fig. 12 seems less than the negative peak value of raw p in Fig. 10 by about 30 Pa due to the conditional averaging. Now, we consider this, more precisely. Figure 13 shows six pressure distributions during one impeller-rotation period at $2r/D_2 = 0.62$ and $Re = 8.0\times10^3$ with the tongue. The six distributions are selected at random among twenty distributions used for averaging. We can see that each one-period distribution of raw p attains the minimum value of about -50 Pa, which is consistent with Fig. 10. However, the position of θ for the minimum p varies in a range about 200 – 300 deg. This variation is considered to be a main reason for the increase of the minimum value of p_{PA}. We can observe the variation at $2r/D_2 \gtrsim 0.5$ and for $Re \gtrsim 6.0\times10^3$. On the other hand, we cannot observe the variation at $2r/D_2 \lesssim 0.5$ or for $Re \lesssim 6.0\times10^3$, where the increase by the conditional averaging is negligible. –We can also observe higher-frequency fluctuations with a period of about 13 deg. The corresponding frequencies to such fluctuations are about 120 Hz.–

Figure 14 shows The time-mean pressure coefficient C_{pmean} with the tongue plotted against Re at various positions of $2r/D_2$. We can see that C_{pmean} decreases with increasing Re and that C_{pmean} approaches zero. So, C_{pmean} is approximately zero for $Re \gtrsim 4.0\times10^3$, being independent of Re.

Figure 15 shows The time-mean pressure coefficient C_{pmean} without the tongue plotted against Re. We can see that the result well coincides with that with tongue in Fig. 14. This suggests that the influences of the tongue insertion upon time-mean flow fields seen insignificant.

4. Conclusions

To clarify the characteristics of the flow around and inside a cross-flow impeller in a typical geometry, over a wide parameter range of an aspect ratio L/D_2, we have observed the flow. In order to eliminate the complicated casing factors, the impeller rotates in open space without any casings. As a result, using hot wire anemometer measurements and using conventional flow visualisations, we detect the eccentric-vortex revolution inside the impeller. Then, we divide the flow around the impeller into three areas. Besides, using a particle image velocimetry technique, we quantitatively show spatial distributions, whose accuracy is checked in comparison with the hot-wire-anemometer results. Then, we have defined the outflow rate Q_o out of the impeller and the maximum vorticity ω_{max}. To conclude, both the L/D_2 effects upon Q_o and ω_{max} are not negligible, when L/D_2 is less than unity. And, both Q_o and ω_{max} attain the maximum values for $L/D_2 = 0.6$. From a practical point of view, these results suggest a possibility of more efficient impellers, when we use the optimum aspect ratio of $L/D_2 = 0.6$. In order to investigate the aspect-ratio effect, we further reveal minute fluctuating pressures on an impeller end wall for a singular $L/D_2 = 0.6$. Especially in these pressure measurements, the eccentric vortex is prevented to revolute by the insertion of a tongue, in order to consider the spatial structure of flow more precisely. Strictly speaking, the eccentric vortex is not completely fixed, but fluctuate in azimuthal direction with an amplitude of $\theta \approx \pm50$ deg. for $2r/D_2 \geq 0.50$ and the Reynolds number $Re \gtrsim 6.0\times10^3$. We have confirmed such a Reynolds number Re effect as the time-mean pressure coefficient C_{pmean} decreases with increasing Re for $Re \lesssim 4.0\times10^3$. Furthermore, we have confirmed that the influence of the tongue insertion upon the Re effect is negligible.

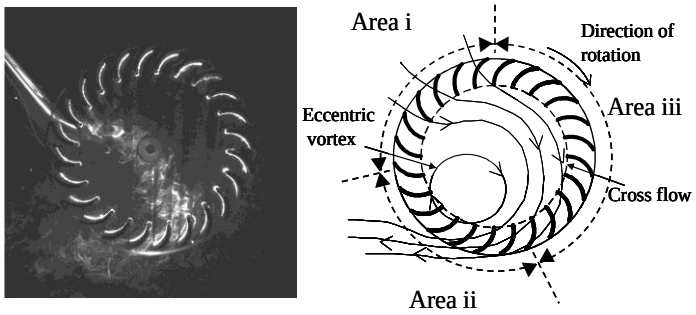

Fig. 4 Visualised flow by smoke (L/D_2 = 1.0, Re = 2.5×10^3). i, Inflow area; ii, outflow area; iii, less-flow area.

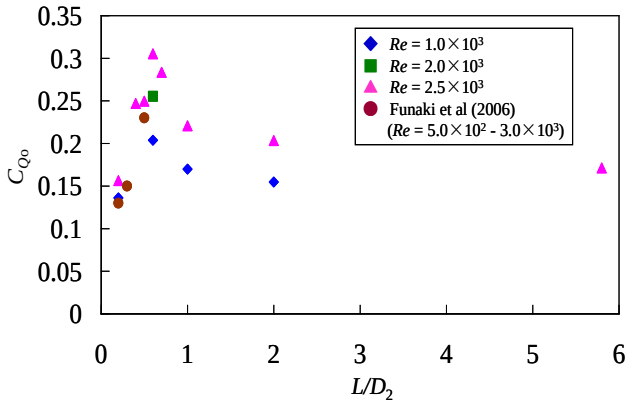

Fig. 5 Outflow-rate coefficient C_{Qo} against aspect ratio L/D_2 (L/D_2 = 0.2 – 5.8, Re = 1.0×10^3, 2.0×10^3, 2.5×10^3).

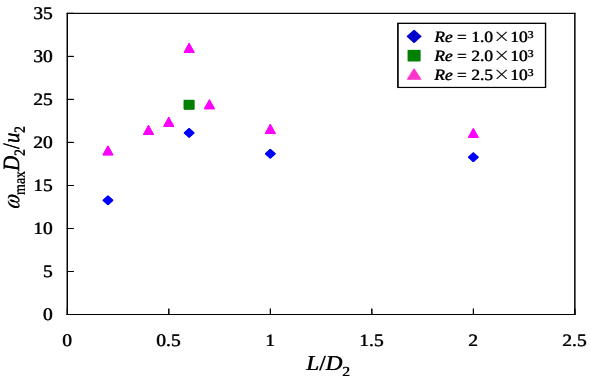

Fig. 6 The normalised maximum vorticity $\omega_{max}D_2/u_2$ inside an impeller against aspect ratio L/D_2 (L/D_2 = 0.2 – 1.0, Re = 1.0×10^3, 2.0×10^3, 2.5×10^3).

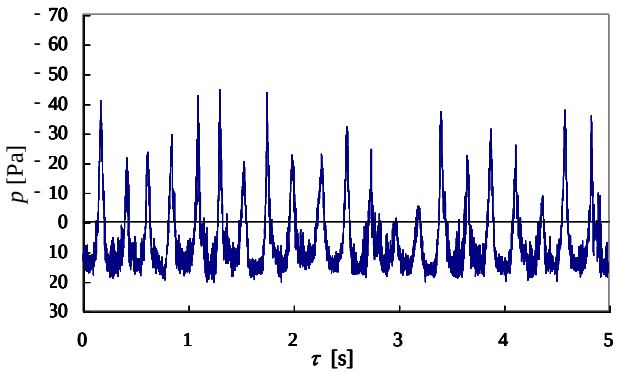

Fig. 7 Time history of the pressure-sensor signal at $2r/D_2$ = 0.62 for Re = 8.0×10^3 without the tongue.

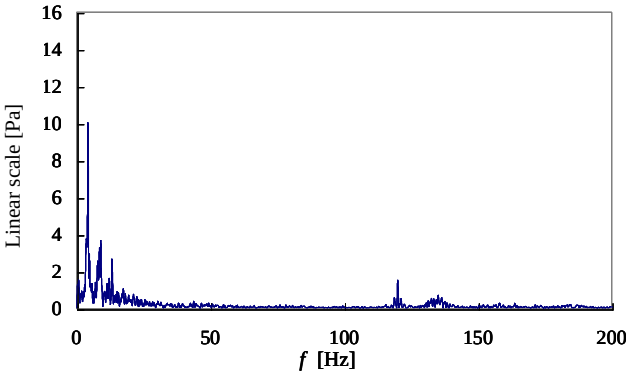

Fig. 8 Spectrum of the pressure-sensor signal at $2r/D_2$ = 0.62 for Re =8.0×10^3 without the tongue.

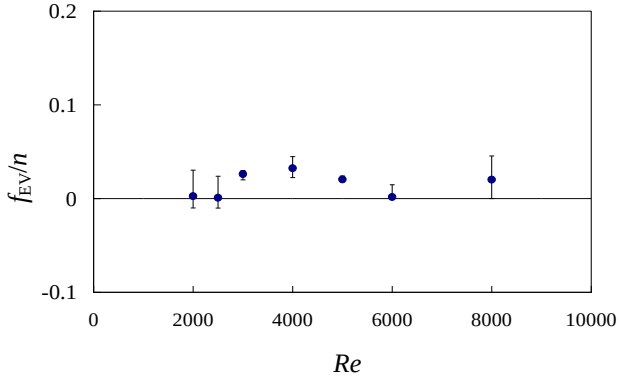

Fig. 9 Normalised eccentric-vortex-revolution frequency f_{EV}/n against Re without the tongue at $2r/D_2$ = 0.22 – 0.62.

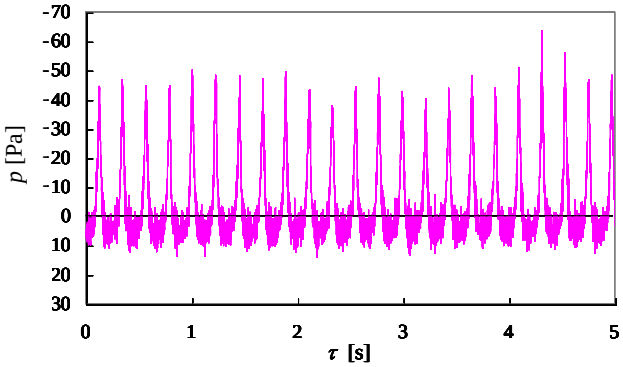

Fig. 10 Time history of the pressure-sensor signal at $2r/D_2$ = 0.62 for Re = 8.0×10^3 with the tongue.

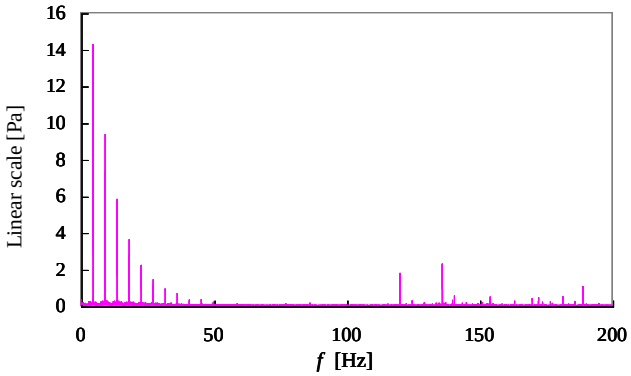

Fig. 11 Spectrum of the pressure-sensor signal at $2r/D_2$ = 0.62 for Re = 8.0×10^3 with the tongue.

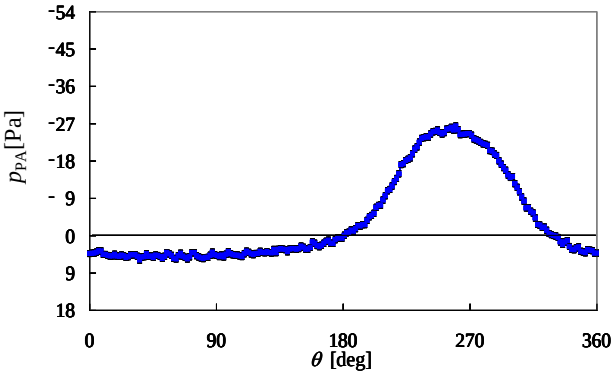

Fig. 12 Phase-averaged pressure distribution during one impeller-rotation period at $2r/D_2$ = 0.62 and Re = 8.0×10^3 with the tongue.

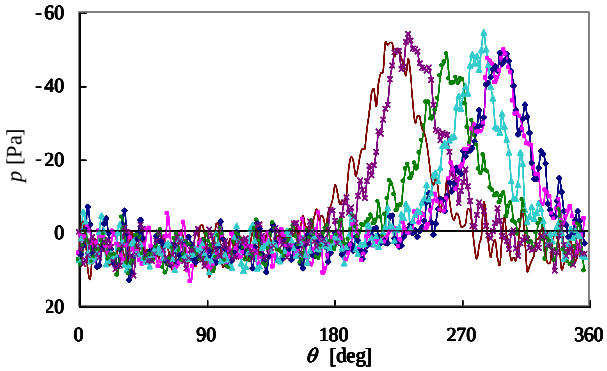

Fig. 13 Superimposed pressure distributions during one impeller-rotation period at $2r/D_2$ = 0.62 and Re = 8.0×10^3 with the tongue. Diamond, 1st period; square, 2nd period; triangle, 5th period; circle, 10th period; cross, 15th period; bar, 20th period.

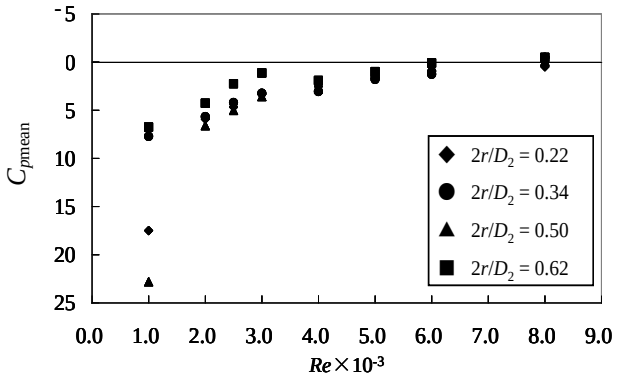

Fig. 14 Time-mean pressure coefficient $C_{p\text{mean}}$ against Reynolds number Re with the tougue.

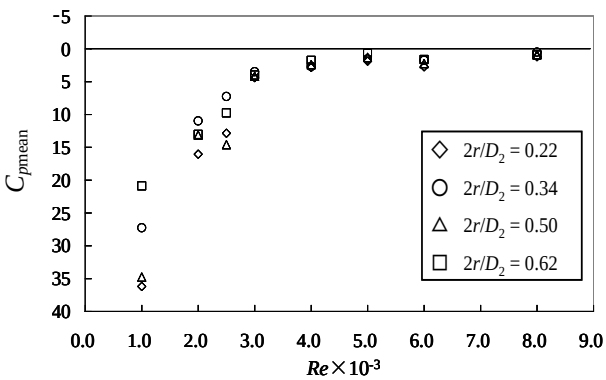

Fig. 15 Time-mean pressure coefficient $C_{p\text{mean}}$ against Reynolds number Re without the tongue.

Nomenclature

c	: chord length of a blade	[mm]
C_{Qo}	: outflow-rate coefficient	
C_p	: pressure coefficient	
D_1	: inner diameter	[mm]
D_2	: outer diameter (= length scale)	[mm]
f	: frequency	[Hz]
f_{EV}	: frequency of eccentric-vortex revolution	[Hz]
L	: impeller length, span	[mm]
n	: impeller rotation speed	[Hz]
P	: pitch between blades	[mm]
p	: pressure	[Pa]
Q_o	: outflow rate	[m^3/s]
r	: radial coordinate	[m]
Re	: Reynolds number ($\equiv nD_2^2/2$)	
t	: blade thickness	[mm]
u	: flow velocity	[m/s]
u_2	: impeller outer-periphery velocity	[m/s]
Z	: number of blade	
β_1	: inner angle of a blade	[deg.]
β_2	: outer angle of a blade	[deg.]
ν	: kinematic visconsity	[m^2/s]
τ	: time	[s]
θ	: azimuthal coordinate	[deg.]
L/D_2	: aspect ratio	
ω_{max}	: maximum vorticity	[1/s]

Subscripts

PA : phase-avaraged
mean : time-mean

References

[1] Eck, B., 1973, "Fans –Design and Operation of Centrifugal, Axial-Flow and Cross-Flow Fans–," Pergamon Press, Oxford.
[2] Porter, A. M. and Markland, E., 1970 "A Study of the Cross Flow Fan," J. Mechanical Engineering Science, Vol. 12, No. 6, pp. 421-431.
[3] Yamafuji, K., 1975, "A Study on Cross-Flow-Impeller Flow –1st Report, Experimental Study–," Trans. JSME, Ser. II, Vol. 41, No. 341, pp. 189-199 (in Japanese).
[4] Yamafuji, K., 1975, "A Study on Cross-Flow-Impeller Flow –2nd Report, Analytical Study–," Trans. JSME Ser. II, Vol. 41, No. 344, pp. 1184-1192 (in Japanese).
[5] Murata, S. and Nishihara, K., 1975a, "A Study on Cross-Flow Impeller –1st Report, Effect of Casing Geometry on Impelle's Performance–," Trans. JSME, Ser. II, Vol. 41, No. 347, pp. 2062-2075 (in Japanese).
[6] Murata, S. and Nishihara, K., 1975b, "A Study on Cross-Flow Impeller –2nd Report, Performance Characteristics and Inside Flow–," Trans. JSME, Ser. II, Vol. 41, No. 347, pp. 2076-2089 (in Japanese).
[7] Nakamura, K. and Okutani, K., 1983, "An analysis on Flow inside Cross-Flow Fan," Turbomachinery, Vol. 11, No. 4, pp. 10-15 (in Japanese).
[8] Nakamura, K., Umekage, Y., Tomohiro, T. and Okutani, K., 1986, "An Automatic Measurement and an Analysis for Flow inside Cross-Flow Fan," Turbomachinery, Vol. 14, No. 2, pp. 9-18 (in Japanese).
[9] Takushima, A. and Iizuka, K., 1992, "Numerical Analysis of Cross-Flow Fan by a Clouds-in-Cells Method Combined with the Finite-Element Method," Trans. JSME, Ser. B, Vol.58, No. 545, pp. 64-70 (in Japanese).
[10] Fukano, T., Yamashita, Y., Hara, Y., Kinoshita, K. and Nomiyama, S., 1992, "Reduction of Noise Generated by a Cross Flow Fan –Part 1: The Effect of Geometries of a Tangue and a Rotor–," Turbomachinery, Vol. 20, No. 8, pp. 22-28 (in Japanese).
[11] Fukano, T., Yamashita, Y., Hara, Y. and Kinoshita, K., 1993a, "Reduction of Noise Generated by a Cross Flow Fan –Part 2: The Effect of the Clearance between a Tongue and a Rotor–," Turbomachinery, Vol. 21, No. 8, pp. 16-22 (in Japanese).
[12] Fukano, T., Yamashita, Y., Hara, Y., Kinoshita, K., 1993b, "Reduction of Noise Generated by a Cross Flow Fan –Part 3: The Effect of Geometry of a Scroll–," Turbomachinery, Vol. 21, No. 8, pp. 11 – 17 (in Japanese).
[13] Tsurusaki, H., Shimizu, H., Tsujimoto, Y., Yoshida, Y. and Kitagawa, K., 1993, "Study of Cross-Flow-Fan Internal Flow by Flow Visualization –1st Report, Discussion of Measured Results by Particle Tracking Velocimetry–," Trans. JSME, Ser. B, Vol. 59, No. 568, pp. 3743-3748 (in Japanese).
[14] Fukano, T., Yamashita, Y., Hara, Y., Kinoshita, K., 1994, "Reduction of Noise Generated by a Cross Flow Fan –Part 4: Relation between Flow Pattern and Performance–," Turbomachinery, Vol. 21, No. 8, pp. 18-23 (in Japanese).
[15] Tsurusaki, H., Shimizu, H., Tsujimoto, Y., Yoshida, Y. and Kitagawa, K., 1997, "Visualization Measurement and Numerical Analysis of Internal Flow in Cross-Flow Fan," Trans. ASME, J. Fluids Engineering, Vol. 119, pp. 633-638.
[16] Lazzaretto, A., 2003a, "A Criterion to Define Cross-Flow Fan Design Parameters," Trans. ASME, J. Fluids Engineering, Vol. 125, pp. 680-683.
[17] Lazzaretto, A., Toffolo, A. and Martegani, A. D., 2003b, "A Systematic Experimental Approach to Cross-Flow Fan Design," Trans. ASME, J. Fluids Engineering, Vol. 125, pp. 684-693.
[18] Toffolo, A., Lazzaretto, A. and Martegani, A. D., 2004, "An Experimental Investigation of the Flow Field Pattern within the Impeller of a Cross-Flow Fan," Experimental Thermal and Fluid Science, Vol. 29, pp. 53-64.
[19] Toffolo, A., 2005, "On the Theoretical Link between Design Parameters and Performance in Cross-Flow Fans: a Numerical and Experimental Study," Computers and Fluids, Vol. 34, pp. 49-66.
[20] Go-Long, T., Tsung-Heisen, T., Tung-Chen, L. and Kuang-Hsieng, W., 2006, "Flow Style Investigation and Noise Reduction of a Cross-Flow Fan with Varied Rotor-Skew-Angle Rotor," JSME Int. J., Ser. B, Vol. 49, No. 3, pp. 1197-1205.
[21] Casarsa, L. and Giannattasio, P., 2011, "Experimental Study of the Three-Dimensional Flow Field in Cross-Flow Fans,"

Experimental Thermal and Fluid Science, Vol. 35, pp. 948-959.
[22] Dang, T. Q. and Bushnell, P. R., 2009, "Aerodynamics of cross flow fans and their application to aircraft propulsion and flow control," Progress in Aerospace Sciences, Vol. 45, pp. 1-29.
[23] Yu, H. T., Hobson, G. V.,Gannon, A. J. and Platzer, M., 2008, "Experimental investigation and numerical prediction of the performance of a cross flow fan," Proceedings of the 12th International Symposium on Transport Phenomena and Dynamics of Rotating Machinery, Honolulu, Hawaii, USA.
[24] Funaki, J., Kimata, N., Hisada, M. and Hirata, K., 2006, "Aspect-Ratio and Reynolds-Number Effects on Short-Span Cross-Flow Impellers without Casings," JSME Int. J., Ser. B, Vol. 49, No. 4, pp. 1197-1205.
[25] Hirata, K., Iida, Y.,Takushima, A. and Funaki, J., 2008, "Instantaneous Pressure Measurement on a Rotating Blade of Cross-Flow Impeller," J. Environment and Engineering, JSME, Vol. 3, No. 2, pp. 261-271.